JACS
JOURNAL OF THE AMERICAN CHEMICAL SOCIETY

Article

pubs.acs.org/JACS

Model of a Six Immunoglobulin-Like Domain Fragment of Filamin A (16−21) Built Using Residual Dipolar Couplings

Helena Tossavainen,[†,#] Outi Koskela,[‡,#] Pengju Jiang,[§,∥] Jari Ylänne,[⊥] Iain D. Campbell,[§] Ilkka Kilpeläinen,[‡] and Perttu Permi*[,†]

[†]Program in Structural Biology and Biophysics, Institute of Biotechnology, University of Helsinki, Viikinkaari 1, P.O. Box 65, FI-00014 Helsinki, Finland

[‡]Laboratory of Organic Chemistry, Department of Chemistry, University of Helsinki, P.O. Box 55, FI-00014 Helsinki, Finland

[§]Biochemistry Department, University of Oxford, Oxford, OX1 3QU United Kingdom

[∥]School of Pharmaceutical Engineering & Life Science, Changzhou University, Changzhou, 213164 China

[⊥]Department of Biological and Environmental Science and Nanoscience Center, University of Jyväskylä, P.O. Box 35, FI-40014 Jyväskylä, Finland

Supporting Information

ABSTRACT: Filamins are actin-binding proteins that participate in a wide range of cell functions, including cell morphology, locomotion, membrane protein localization, and intracellular signaling. The three filamin isoforms found in humans, filamins A, B, and C, are highly homologous, and their roles are partly complementary. In addition to actin, filamins interact with dozens of other proteins that have roles as membrane receptors and channels, enzymes, signaling intermediates, and transcription factors. Filamins are composed of an N-terminal actin-binding domain and 24 filamin-type immunoglobulin-like domains (FLN) that form tail-to-tail dimers with their C-terminal FLN domain. Many of the filamin interactions including those for glycoprotein Ibα and integrins have been mapped to the region comprising FLN domains 16−21. Traditionally, FLN domains have been viewed as independent folding units, arranged in a linear chain joined with flexible linkers. Recent structural findings have shown that consecutive FLNs form more intricate superstructures. The crystal structure of filamin A domains 19−21 (FLNa19−21) revealed that domains 20 and 21 fold together and that the domain interaction can be autoregulatory. The solution structure of domains 18−19 showed a similar domain interaction, whereas domain pair 16−17 has a completely different domain packing mode. In this study, we characterize the domain organization of the FLNa domain sextet 16−21 using NMR spectroscopy. A structure model of this 60-kDa protein has been built using residual dipolar coupling restraints. RDCs and ^{15}N relaxation data have been used to characterize interdomain motions.

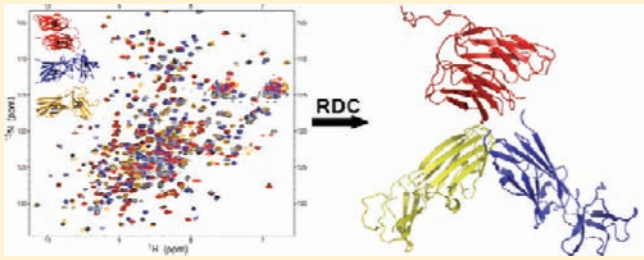

INTRODUCTION

Filamins organize actin filaments into cross-linked networks and thick bundles.[1] Three highly homologous filamin isoforms are found in humans: filamins A, B, and C. Filamins A and B have partly overlapping tissue expression profiles and function whereas the expression and functions of filamin C are mostly restricted to skeletal muscle. Filamin A is the most abundant and uniformly expressed isoform and is the most studied. Filamins are essential for normal vertebrate development, and mutations in filamins cause congenital disorders in the brain, bone, limbs, and the cardiovascular system.[2−4] In addition to actin, filamins have numerous other interaction partners that have versatile roles as cell membrane receptors, enzymes, intracellular signaling intermediates, and transcription regulators.[5] The diverse physiological consequences of filamin point mutations are thought to manifest different filamin interactions.

Filamins are large proteins (MW 280 kDa) that have a modular structure (Figure 1). A filamin monomer is composed of an N-terminal actin-binding domain (ABD) and 24 filamin-type immunoglobulin-like domains (FLN).[6] Filamins form tail-to-tail dimers through their C-terminal FLN domain, which enables physical cross-linking of the actin filaments.[7] The first structures of filamin ABDs were recently solved,[8,9] and they closely resemble the ABDs of α-actinin and spectrin. FLN domains (called FLN here) form two rod regions, rod 1 and rod 2, interrupted by flexible hinges. Electron microscopic images of filamins show a flexible elongated dimer with a total length of approximately 160 nm.[10] FLNs fold into a β sandwich structure with seven antiparallel β strands. Several structures of isolated single FLNs are available in the Protein Data Bank, and the published structures of FLNs with bound ligands suggest that the C strand is a general interaction site.[11−15]

Received: December 8, 2011
Published: March 28, 2012

   dx.doi.org/10.1021/ja2114882 | J. Am. Chem. Soc. 2012, 134, 6660−6672

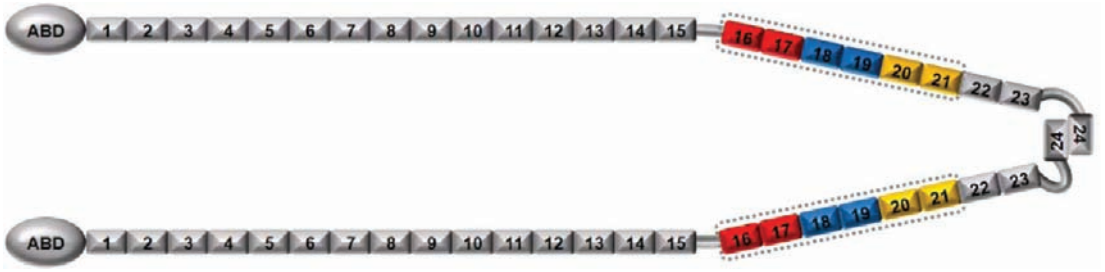

Figure 1. Schematic structure of the filamin dimer and the location of the domains investigated in this study. Filamins are composed of an N-terminal actin-binding domain and 24 filamin-type immunoglobulin-like (Ig) domains. The Ig domains form two rod regions, rod 1 (Ig domains 1–15) and rod 2 (Ig domains 16–23), interrupted by two flexible hinges. Filamin monomers form tail-to-tail dimers through interactions in the 24th Ig domain. The ABD, actin-binding domain is shown as an ellipse, the immunoglobulin-like domains are rectangles and the bold lines indicate hinge regions. The Ig domain pairs are color coded as follows: FLNa16–17, red; FLNa18–19, blue; FLNa20–21, yellow. The same color coding is used for the domain pairs in other figures in this article. The dashed line encloses the FLNa16–21 domain sextet.

FLNs were believed to arrange themselves into a linear flexible chain of independent domains[16] but electron microscopic images of filamin constructs suggest that the C-terminal domains form a more compact superstructure.[17] Structures of multidomain constructs 16–17, 18–19, and 19–21 of filamin A (FLNa16–17, FLNa18–19, and FLNa19–21) also revealed unexpected interdomain organization and tight domain interactions in these domain pairs.[18,19] The even-numbered domains, 16, 18, and 20, all lack the first β strand (A strand) of the consensus FLN fold. In FLNa18–19 and 20–21, the A strand of the even-numbered domain forms an additional strand next to strand C of the following odd-numbered domain; the A strand is found to be unstructured in FLNa16. FLNa18–19 and 20–21 form similar orthogonal T-shaped domain pairs whereas FLNa16–17 are bound together in an antiparallel orientation with their β sheets roughly parallel. As the N- and C-termini of FLNa18–19 and 20–21 come close in space, it seems likely that the domains within FLNa16–21 will pack into a compact cluster. Since the interaction sites of several filamin interaction partners have been mapped to FLNa16–21,[20] the domain arrangement could potentially affect these interactions.

NMR spectroscopy is a versatile tool in structural studies of multidomain proteins.[21] Crystallization of modular proteins for X-ray diffraction studies is often hampered by interdomain dynamics. NMR studies of modular proteins are complicated by the fast transverse relaxation of these large molecules, but sample perdeuteration, together with transverse relaxation-optimized spectroscopy (TROSY)[22] can be exploited to alleviate this problem. As NOE-based distance restraints are often scarce across dynamic interdomain interfaces, additional conformational restraints can be introduced to gain adequate structural information. Paramagnetic relaxation enhancements (PREs)[23,24] and residual dipolar couplings (RDCs)[25−27] provide long-range structural information as well as a means to explore interdomain dynamics.

In this work, we have used RDC restraints to study the organization of a six domain fragment of filamin A, consisting of domains 16–21 (FLNa16–21, Figure 1). Extensive backbone chemical shift assignments of FLNa16–21 were accomplished using sample perdeuteration and TROSY-based triple-resonance spectra. A 3D MQ-HNCO TROSY[28] spectrum was recorded to extract 430 ^{1}HN–^{15}N RDCs. Using the previously published structures of FLNa domain pairs 16–17, 18–19,[19] and 20–21,[18] we built a model of the 60-kDa FLNa16–21 domain sextet through rigid-body modeling. To our knowledge, this is one of the largest multidomain protein structures, in terms of molecular weight and number of structural modules that have been modeled using RDC restraints from NMR studies. The RDC data recorded for FLNa16–21 gives new insight into the domain organization of FLNa18–19 and 20–21. Relaxation analysis was used to give additional information about the interdomain dynamics.

EXPERIMENTAL DETAILS

NMR Spectroscopy, Experiments and Data Analysis. Expression and purification of the ^{2}H/^{13}C/^{15}N-labeled FLNa16–21 have been described previously.[28] The double-labeled ^{13}C/^{15}N FLNa20–21 (residues 2142–2329) sample was prepared as described earlier.[18] For the NMR experiments, the ^{2}H/^{13}C/^{15}N-labeled FLNa16–21 sample was concentrated to a final protein concentration of 0.5 mM. The protein concentration of ^{13}C/^{15}N-labeled FLNa20–21 was 1 mM. Samples were buffered to pH 6.8 with 50 mM of sodium phosphate. In addition, the samples contained 100 mM NaCl, 1 mM DTT, and 2 mM sodium azide. The D_2O concentration of the sample solution was 7% (v/v). All NMR spectra were recorded at 30 °C.

The NMR spectra of ^{13}C/^{15}N-labeled FLNa20–21 and ^{2}H/^{13}C/^{15}N-labeled FLNa16–21 were recorded on Varian Unity INOVA 600 and 800 MHz NMR spectrometers, equipped with a ^{1}H/^{13}C/^{15}N triple-resonance probehead and an actively shielded XYZ triple-axis gradient system. Spectra were processed using the standard VNMRJ 2.1 revision B software package and analyzed using Sparky 3.110.[29] Chemical shifts were referenced to TSP indirectly using the water signal as an internal reference. The spectra used for the sequential backbone resonance assignment of ^{13}C/^{15}N-labeled FLNa20–21 were ^{1}H,^{15}N-HSQC, HNCA, HN(CO)CA, HNCACB, HN(CO)CACB, and CC(CO)NH. The backbone resonance assignment of ^{2}H/^{13}C/^{15}N-labeled FLNa16–21 was done using the TROSY versions of the ^{1}H,^{15}N-HSQC, HNCA, HN(CO)CA, and HNCACB spectra. The backbone amide ^{15}N T_1 and T_2 relaxation time spectra as well as steady-state {^{1}H}-^{15}N heteronuclear NOEs of ^{2}H/^{13}C/^{15}N-labeled FLNa16–21 were measured using the TROSY-based implementations of standard relaxation experiments.[30,31] The following delays were used for T_1 times (0.01, 0.11, 0.33, 0.66, 1.1, 1.8, 2.6, 3.5, 4.5, and 6.0 s) and T_2 times (0.01, 0.03, 0.05, 0.07, and 0.09 s). A recycle delay of 5 s was used for both T_1 and T_2 data. Heteronuclear NOEs were measured using an 8 s relaxation delay with and without ^{1}H saturation. T_1s, T_2s and their uncertainties were obtained from exponential fits to the decaying peak intensities, as implemented in Sparky. Heteronuclear NOE values were determined as the peak intensity ratio observed in NOE spectra acquired with and without ^{1}H saturation. An estimate of the error was obtained from the rms noise in the two spectra. All other uncertainties were obtained by error propagation. Fitting of relaxation data to the model structure was done with the program TENSOR 2.[32]

dx.doi.org/10.1021/ja2114882 | J. Am. Chem. Soc. 2012, 134, 6660–6672

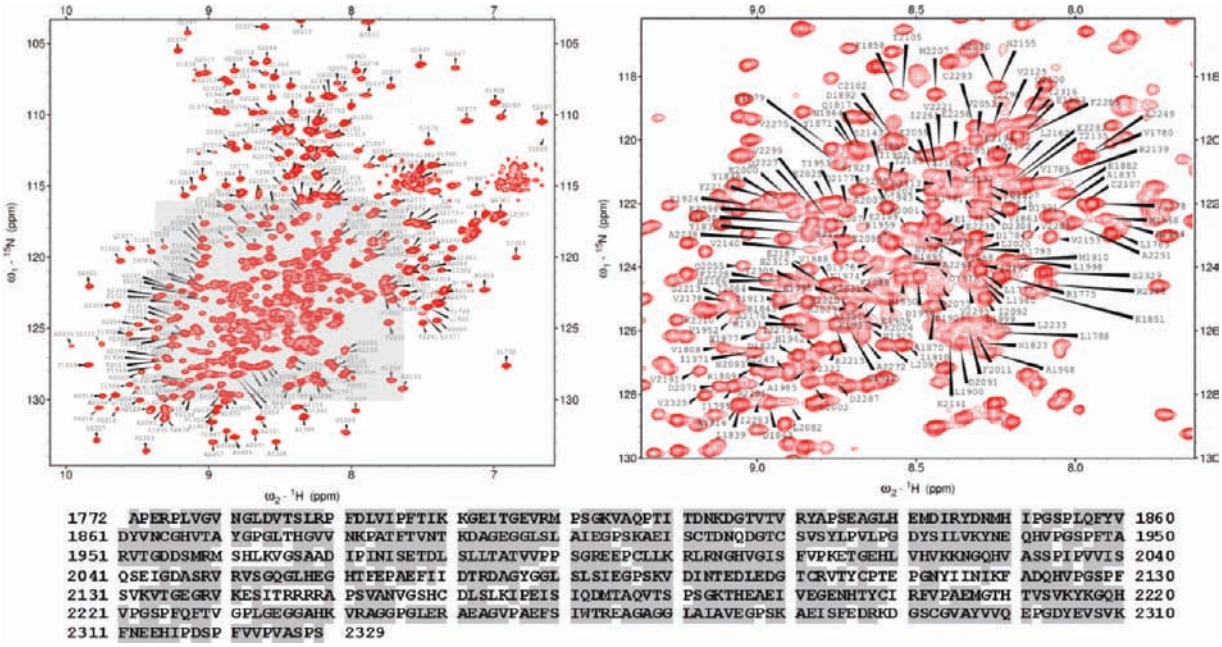

Figure 2. $^{1}H,^{15}N$-HSQC-TROSY spectrum of $^{2}H,^{13}C,^{15}N$-labeled FLNa16−21 (FLNa residues 1772−2329). The left panel shows the entire spectrum and right panel is an expansion of the gray shaded area. Around 88% of all backbone N−H groups were detected in the $^{1}H,^{15}N$-HSQC spectrum and assigned. The peaks are labeled with their assignments. The lower panel shows the sequence of the FLNa16−21 construct and the location of the assigned residues (gray shading).

To measure residual dipolar couplings, $^{2}H/^{13}C/^{15}N$-labeled FLNa16−21 was aligned with Pf1 phage alignment media[33] purchased from Asla Biotech Ltd. The phage concentration of the aligned sample was 15 mg/mL, and the protein concentration was 0.4 mM. Scalar and residual dipolar couplings between amide proton (^{1}HN) and nitrogen (^{15}N) were measured using a modified three-dimensional HNCO-TROSY -based triple-resonance experiment.[28] The MQ-HNCO-TROSY experiment employs a HMQC-like coherence transfer from ^{15}N to $^{13}C'$ and enables labeling of the ^{15}N chemical shift with higher resolution compared to the INEPT type $^{15}N-^{13}C'$ transfer used in the conventional HNCO-TROSY experiment. Based on attainable ^{1}HN and ^{15}N linewidths for the TROSY and semi-TROSY, as well as decoupled components in FLNa16−21, we decided to measure $^{1}HN-^{15}N$ couplings from the separation of the TROSY component and the decoupled $^{15}N-^{1}HN$ cross peak in the ^{15}N dimension. The MQ-HNCO-TROSY spectra both in water and phage were acquired using four transients per FID with 40, 128, and 853 complex points, corresponding to acquisition times of 18.2, 49.2, and 85.3 ms in t_1, t_2, and t_3, respectively. A longer interscan delay was used for the MQ-HNCO-TROSY spectrum measured in the liquid crystal medium (2.4 vs 1.55 s), resulting in total acquisition times of 80 and 118 h for experiments measured in water and phage, respectively. Data sets for selecting TROSY/TROSY and decoupled/TROSY components in ^{15}N and ^{1}H dimensions were recorded in an interleaved manner. The RDC contribution to the observed splitting in liquid crystal medium was obtained by subtracting the $^{15}N-^{1}HN$ values measured in water from the values obtained in liquid crystal medium.

To identify possible instability of the liquid crystal medium that could induce variation in the alignment tensor, we recorded the deuterium splitting at the beginning and end of the measurements using a single ^{2}H pulse experiment. In both cases a ^{2}H splitting of 14.6 Hz was measured suggesting a highly stable liquid crystal medium.

Rigid-Body Modeling of FLNa16−21 using RDC Restraints. Rigid-body modeling of the FLNa16−21 domain organization was done with the MODULE 2 program.[34] An arbitrary starting structure of FLNa16−21 (residues 1772−2329) was built using the structures of FLNa16−17 (PDB ID code 2K7P, model 1, residues 1772−1955), FLNa18−19 (2K7Q, model 1, residues 1956−2136), and FLNa20−21 (2J3S, chain A, residues 2137−2329) by superimposing the overlapping parts of the substructures.[18,19] The structure was divided into six separate modules according to the domain boundaries so that the A strands of FLNa18 and 20 were included as part of domains 19 and 21, respectively (see Table 1). The observed residual dipolar couplings of the backbone N−Hs were used as restraints in the rigid-body modeling of the FLNa16−21 domain orientations. RDCs of dynamic residues (as evidenced by relaxation analysis) and residues of the domain linkers and interfaces, which have uncertain conformations in the larger construct, were excluded from the analysis (see the Supporting Information, Table S2 for details of selection). RDCs of residues that do not have well-defined coordinates in the FLNa20−21 crystal structure were also excluded. A total of 321 RDCs were successfully fitted (see Table 1). After the alignment tensors were fitted, the domains were transferred into a common alignment frame. Choices about inclusion and exclusion of degenerate orientations were made based on covalent and nonbonded information as well as chemical shift perturbations observed between spectra of isolated domain pairs and the intact FLNa16−21 construct (see Figure 4). Uncertainties in the A_a values were obtained by a Monte Carlo error analysis, as implemented in MODULE 2.

Model structure ensembles were generated with XPLOR-NIH[35] using ensemble averaging combined with rigid body minimization. RDCs, highly ambiguous NOEs[36] between domains from chemical shift perturbation data and radii of gyration of the individual domains[19] as well as the sextet (Ruskamo et al. unpublished data) were used as restraints. FLNa16−17 (residues 1788−1954) was treated as one rigid body whereas FLNa18−21 were allowed to reorient individually (domain 18 included residues 1970−2040, domain 19 residues 1959−1966 (the A-strand) and 2047−2134, domain 20 residues 2152−2230, and domain 21 residues 2140−2148 (the A-strand) and 2236−2327. In total 326 RDCs were included in the simulations. A single alignment tensor was assumed for all the members of the ensemble. As the starting structure we used the model obtained from the rigid body modeling. Ensemble sizes N_e of 1−4 were tested with one hundred ensembles calculated for each N_e.

RESULTS

Chemical Shift Assignment of FLNa20−21. An initial view of the structural arrangement of the six domain fragment

dx.doi.org/10.1021/ja2114882 | J. Am. Chem. Soc. 2012, 134, 6660−6672

FLNa16−21 was obtained by comparing the $^{15}N-^{1}H$ correlation spectra of FLNa16−21 with those of the isolated FLNa domain pairs 16−17, 18−19,[37] and 20−21. The backbone chemical shift assignment of FLNa20−21 was also carried out separately as no assignments for this domain pair were available; the spectral quality obtained from FLNa20−21 was relatively poor, and assignments were only found for approximately 70% of the backbone amides (the assigned $^{15}N-^{1}H$ HSQC spectrum of FLNa20−21 is provided as Supplementary Figure S1 and Supplementary Table S2 lists the backbone ^{1}H, ^{15}N chemical shift assignments of FLNa16−21). In the $^{1}H,^{15}N$-HSQC spectrum signal intensities were nonuniform and many signals were missing: all signals of residues in the A strand of domain 20 (residues 2142−2148) and most signals of the subsequent large loop (residues 2149−2150 and 2156−2162). In addition some signals from residues in strand C of domain 21, next to strand A of domain 20 (residues 2271−2273) were not present. We reasoned that this arises due to μs-ms time scale dynamics inducing severe line broadening. We did not attempt a full structure determination; instead the X-ray structure of FLNa20−21 was used as a starting model in the RDC analysis.

NMR Chemical Shift Perturbation Data Suggest Transient Interactions between the Domain Pairs in FLNa16−21. The $^{1}H,^{15}N$-HSQC-TROSY spectrum of $^{2}H/^{13}C/^{15}N$-labeled FLNa16−21 showed approximately 450 well-resolved cross-peaks with relatively uniform intensities (Figure 2). It is clear that exhaustive deuterium−proton back-exchange of backbone amides had taken place during protein purification. The spectral quality is excellent considering the large size and modular composition of the protein. Using three TROSY-based triple-resonance spectra, HNCA, HN(CO)CA, and HNCACB it was possible to achieve 88% assignment of the of $^{1}H,^{15}N$ resonances of 514 nonproline residues of FLNa16−21.

A comparison of the $^{1}H,^{15}N$-TROSY spectrum of FLNa16−21 with the corresponding spectra from the isolated domain pairs 16−17, 18−19, and 20−21 shows that the spectrum of FLNa16−21 is very similar to the sum of the spectra from the isolated domain pairs (Figure 3) with nearly all signals in the domain pairs retaining same locations. Signals from domain pair 16−17, in particular, remain the same. The most significant differences are observed in the domain pair linker regions. A closer inspection of the chemical shift differences gives clues about the domain interaction interfaces (Figure 4).

The most prominent changes are seen in the CD and EF loops of domain 21 (residues 2274−2282 and 2300−2306, respectively), located near the linker between domain 19 and the A strand of domain 20. Moreover, several residues from FLNa19, which were assigned in FLNa18−19, could not be identified in FLNa16−21, indicating larger chemical shift perturbation or line broadening in FLNa16−21 (see Figure 2, e.g., V2104 and I2116). Most of the absent signals are clustered around residues 2114−2117 at the beginning of strand F, which is located at the C-terminal end of domain 19 but not quite next to the domain linker to FLNa20−21. The rest of the chemical shift changes are concentrated at residues located close to the linkers between the domain pairs. Changes at the linker between domains 16 and 17 (residues 1865−1868) and at the BC loop of domain 17 (residues 1890−1893) are an exception. These residues are located at the N-terminal side of FLNa16−17. One explanation for these subtle chemical shift changes could be the flexibility of the BC loop (clearly evident

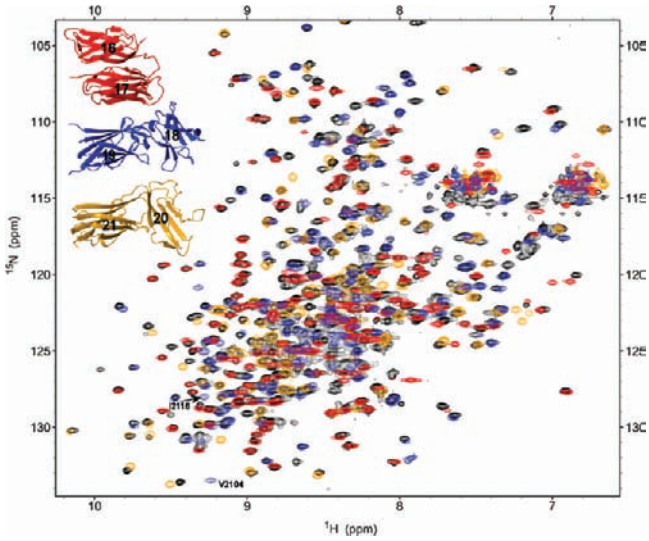

Figure 3. Overlay of FLNa16−21 (black), FLNa16−17 (red), FLNa18−19 (blue), and FLNa20−21 (yellow) $^{1}H,^{15}N$-HSQC spectra. Only minor differences are detected between the spectra of the isolated domain pairs and the spectrum of FLNa16−21, indicating that the internal structures of the domain pairs are conserved in the larger construct. The structures of the isolated domain pairs are shown in the insert. The PDB accession codes of the domain pair structures are FLNa16−17, 2K7P; FLNa18−19, 2K7Q; FLNa20−21, 2J3S.[18,19]

in the relaxation data) leading to a minor conformational adjustment due to slightly different sample conditions. Nevertheless, the chemical shift perturbation mapping indicates that the isolated FLNa domain pairs retain their fold in the six-domain fragment.[18,19,37] The domain pairs also seem to interact mainly *via* the four-residue linker peptides without other stable interactions. However, some of the observed chemical shift changes in the spectra clearly pinpoint domain pair interfaces.

Orientation of Domains in FLNa16−21 using RDCs. The introduction of tunable alignment of biological macromolecules by dissolving them in a dilute liquid crystal medium has paved the way for NMR studies of larger proteins.[38,39] RDCs, which stem from dipolar interactions reintroduced by restricting molecular tumbling using oriented media, depend on the orientation of individual internuclear vectors with respect to the molecular alignment frame and the polarizing magnetic field.[38,40,41] RDCs inherently supply long-distance orientational information, which is extremely helpful in the structure refinement of large proteins which for technical reasons require perdeuteration and therefore have depleted NOE information. RDCs are particularly useful for determining the relative orientation of domains, a persistent problem often encountered in the structure determination of modular proteins. Given that at least five nonredundant RDCs per subunit are available, RDCs can be utilized to unravel the alignment tensor components of the rigid structural unit and consequently to obtain the relative orientation of subunits.[25−27]

In order to study the relative orientation of domains in the 60-kDa domain sextet, we measured $^{1}HN-^{15}N$ RDCs from uniformly $^{15}N/^{13}C/^{2}H$-labeled FLNa16−21 and used the previously published structures of FLNa16−17, 18−19,[19] and 20−21[18] as rigid bodies to build a structure model of FLNa16−21. Measurement of RDCs from a protein with hundreds of residues imposes problems associated with resonance overlap and broad lines, both of which contribute to inaccuracy in determining the alignment tensor from RDCs. To this end, we

dx.doi.org/10.1021/ja2114882 | J. Am. Chem. Soc. 2012, 134, 6660−6672

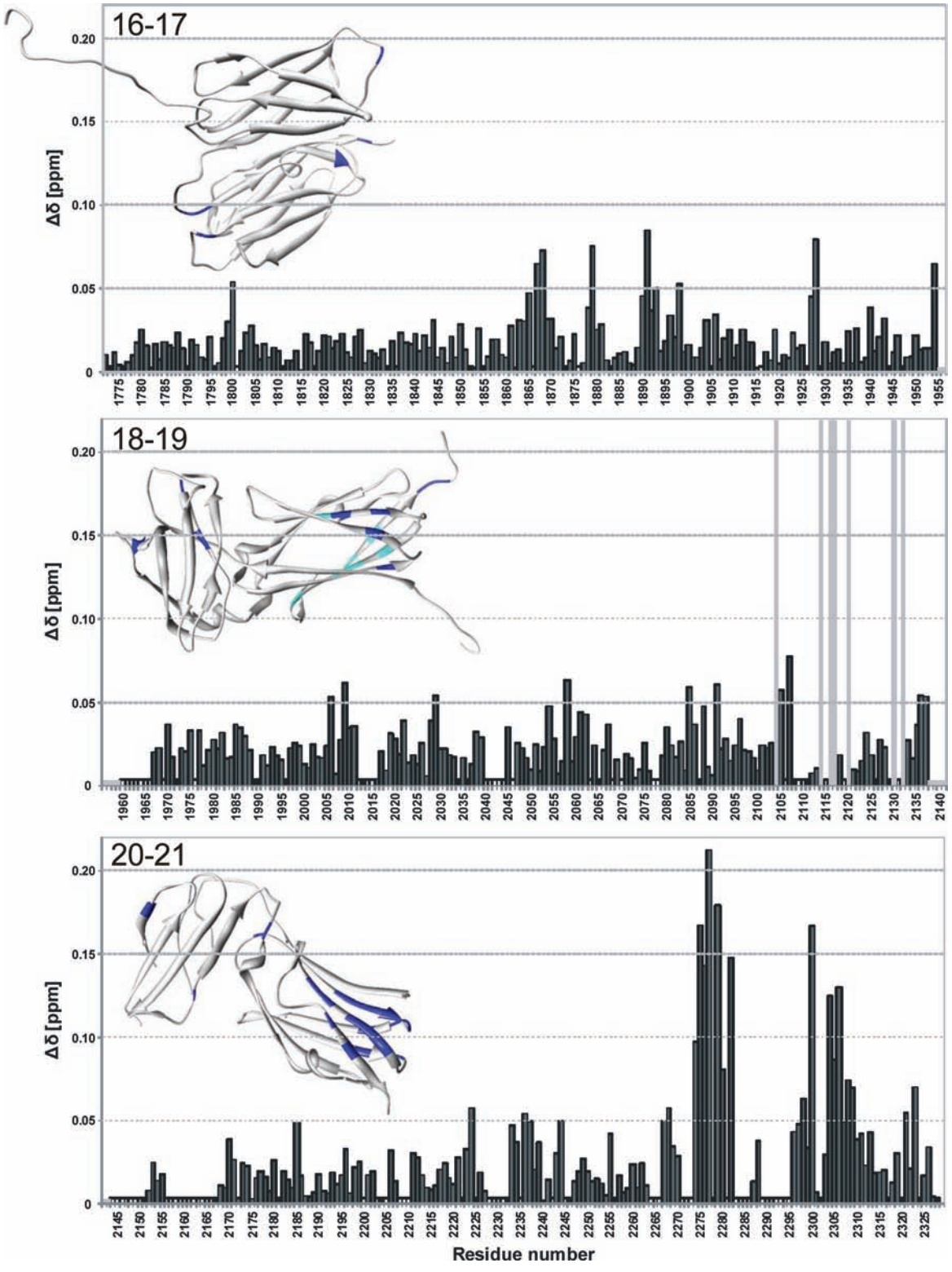

Figure 4. Combined chemical shift differences between the $^{1}H,^{15}N$-HSQC spectra of isolated FLN domain pairs and the spectrum of FLNa16−21. The combined chemical shift differences were calculated using the formula $\Delta\delta = (\Delta\delta H^2 + (0.154 \times \Delta\delta N)^2)^{1/2}$. Only minor shift changes were detected at domain pairs 16−17 and 18−19. The most pronounced changes are seen in domain 21. Several residues of domain 19 that had clearly shifted from their original positions could not be located in the spectrum of FLNa16−21 (e.g., 2104, 2114, 2116, 2117, 2120, 2130, and 2132, gray bars with values set to 0.22, colored in cyan in the structure) (see also Figure 3). Residues lacking assignments either in FLNa16−21 or in the domain pair are marked with gray boxes with black borders. Prolines are marked with black boxes. Domain linkers (gray shaded boxes without borders) are excluded from the plots as large shift differences are detected at these areas by default. Residues with a chemical shift difference ≥ 0.05 ppm are colored in blue in the structures.

dx.doi.org/10.1021/ja2114882 | *J. Am. Chem. Soc.* 2012, 134, 6660−6672

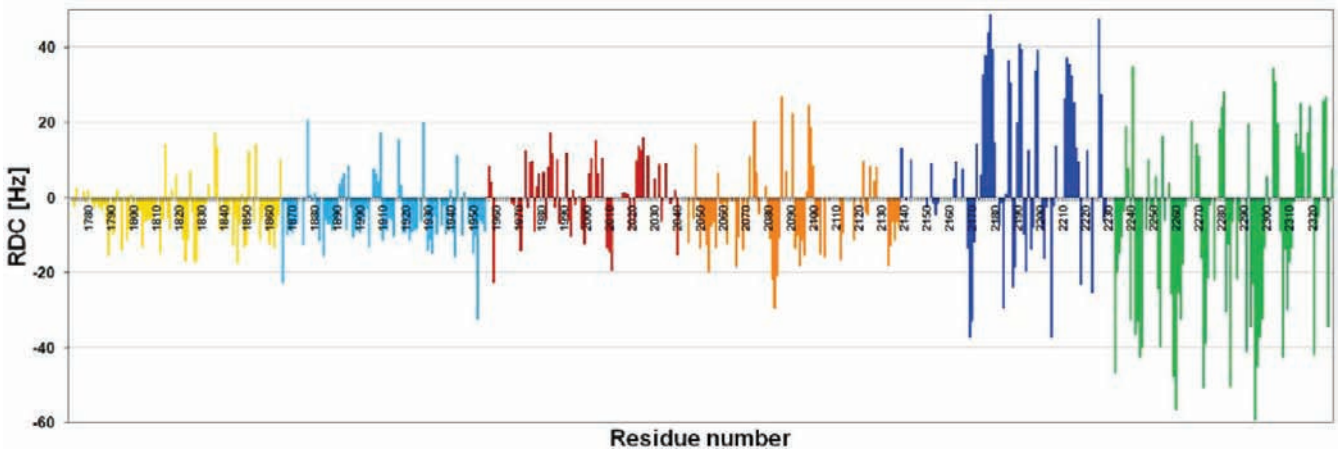

Figure 5. Backbone ^{1}HN−^{15}N RDCs of FLNa16−21. The sequence locations of the constituent domain pairs are color coded as: domain 16, yellow; 17, light blue; 18, red; 19, orange; 20, blue; and 21, green. The couplings are considerably larger for domain pair 20−21, indicating stronger alignment. The uncertainty of the measured RDCs is ±2 Hz.

Table 1. Alignment Tensor Parameters and Estimates of Goodness of RDC Fit of FLNa16−21 Modules[a]

module	N	Q/R_{dip}	Q_{pair}	A_a [$\times10^{-4}$]	A_r [$\times10^{-4}$]	ϑ [$\times10^{-4}$]	ϑ_{int}
1: domain 16 (1772−1865)	65	0.33/0.25	0.33	9.61 ± 0.15	3.20 ± 0.12	10.00 ± 0.15	0.96 ± 0.02
2: domain 17 (1866−1955)	70	0.31/0.23		9.44 ± 0.14	1.95 ± 0.11	9.59 ± 0.14	
3: domain 18 (1969−2043)	41	0.38/0.39	0.40	6.35 ± 0.13	4.00 ± 0.15	7.23 ± 0.13	0.60 ± 0.01
4: domain 19 + A strand of domain 18 (1956−1968, 2044−2138)	56	0.33/0.26		11.81 ± 0.15	2.72 ± 0.14	12.04 ± 0.15	
5: domain 20 (2150−2231)	34	0.24/0.26	0.26	−17.98 ± 0.14	−8.56 ± 0.24	19.45 ± 0.15	0.89 ± 0.01
6: domain 21 +A strand of domain 20 (2139−2149, 2232−2329)	55	0.19/0.19		−21.61 ± 0.11	−4.30 ± 0.20	21.93 ± 0.11	

[a] N: number of RDCs, $Q = \{[\Sigma(RDC_{exp} - RDC_{calc})^2]/[\Sigma(RDC_{exp})^2]\}^{1/2}$;[42] $R_{dip} = [\Sigma(RDC_{exp} - RDC_{calc})^2/N]^{1/2}/RDC_{rms}$, where N is the number of RDCs and $RDC_{rms} = \{2(D_a)^2[4+ 3(A_r/A_a)^2]/5\}^{1/2}$;[43] Q_{pair}, pairwise fit in the final model; A_a: axial component of the alignment tensor; A_r: rhombic component of the alignment tensor; $\vartheta = |A_a|(1 + (3/4)R^2)^{1/2}$, where $R = A_r/A_a$;[46,47] $\vartheta_{int} = \vartheta_a/\vartheta_b$.

employed the three-dimensional MQ-HNCO-TROSY[28] experiment for measuring ^{1}HN−^{15}N RDCs. The experiment provides superior resolution and sensitivity for the measurement of ^{1}HN−^{15}N RDCs in larger proteins and turned out to be a vital component in our ability to obtain 430 ^{1}HN−^{15}N RDCs from this 558-residue protein. However, RDCs for several nonproline residues could not be determined due to missing NH correlations in the ^{1}H,^{15}N-TROSY spectrum or severe overlap with other signals, despite the high-resolution available in the 3D MQ-HNCO TROSY spectrum. A table of the experimental RDCs is provided as Supporting Information (Table S2). The plot of measured RDCs as a function of the FLNa16−21 sequence suggests that the domain pairs align to different extents (Figure 5).

FLNa20−21 appears to align more strongly than FLNa16−17 and 18−19 as rather large RDCs were detected, ranging from −60 to +50 Hz. Most of the ^{1}HN−^{15}N RDCs in domains 16−19 varied between −20 and +20 Hz. The RDC pattern follows the regular β strand topology of the FLN domains, where the HN−N bond vectors are roughly parallel. Domains 16 and 17 show a mutually similar pattern of RDCs, reflecting the nearly parallel orientation of all the β strands in this domain pair. The histogram of the distribution of the RDCs shows that −8 Hz is the most populated value, but also that the distribution is wide, different ^{15}N−^{1}H vector orientations are well represented. In the domain pairs 18−19 and 20−21, the β sheets of the two domains are arranged perpendicularly as shown by the opposite signs of the RDC values for the β strand regions of the two domains.

We initially built a model for the FLNa16−21 fragment from the existing NMR and X-ray structures by superimposing the overlapping parts of the substructures. However, the correlation between observed and back-calculated RDCs from that structure was poor. The Q factor which reports on the goodness of fit[42] was 0.83. Fits with Q factors below 0.4 are considered good. For rigid-body modeling, the starting structure of FLNa16−21 was then divided into "modules" 1−6 corresponding to the different FLNa domains. Considering that the A strands of domains 18 and 20-fold as part of domains 19 and 21, respectively, they were included in the corresponding modules (Table 1). Hereafter, domain 19 (21) refers to a structure including strand A of domain 18 (20).

Several RDCs were excluded from the analysis based on fast internal dynamics manifested by low heteronuclear {^{1}HN}-^{15}N NOEs (see below) or structural uncertainty (e.g., of loop residues). Some RDCs were excluded after initial trials of alignment tensor fitting had shown that they would give very large violations (see the Supporting Information, Table S2 for details). A total of 321 RDCs, 34−70 RDCs per module, were included in the rigid-body modeling. Statistics of the fits are presented as numerical values in Table 1 and graphically in Figure 6A.

Linear correlations between experimental and back-calculated RDCs for individual domains are very good. The alignment tensor components of domains 16 and 17 are nearly identical, and the Q factors for individual domains, as well as for the module pair, are similar, confirming that this fragment behaves as a tightly bound double-domain. This intimate

dx.doi.org/10.1021/ja2114882 | J. Am. Chem. Soc. 2012, 134, 6660−6672

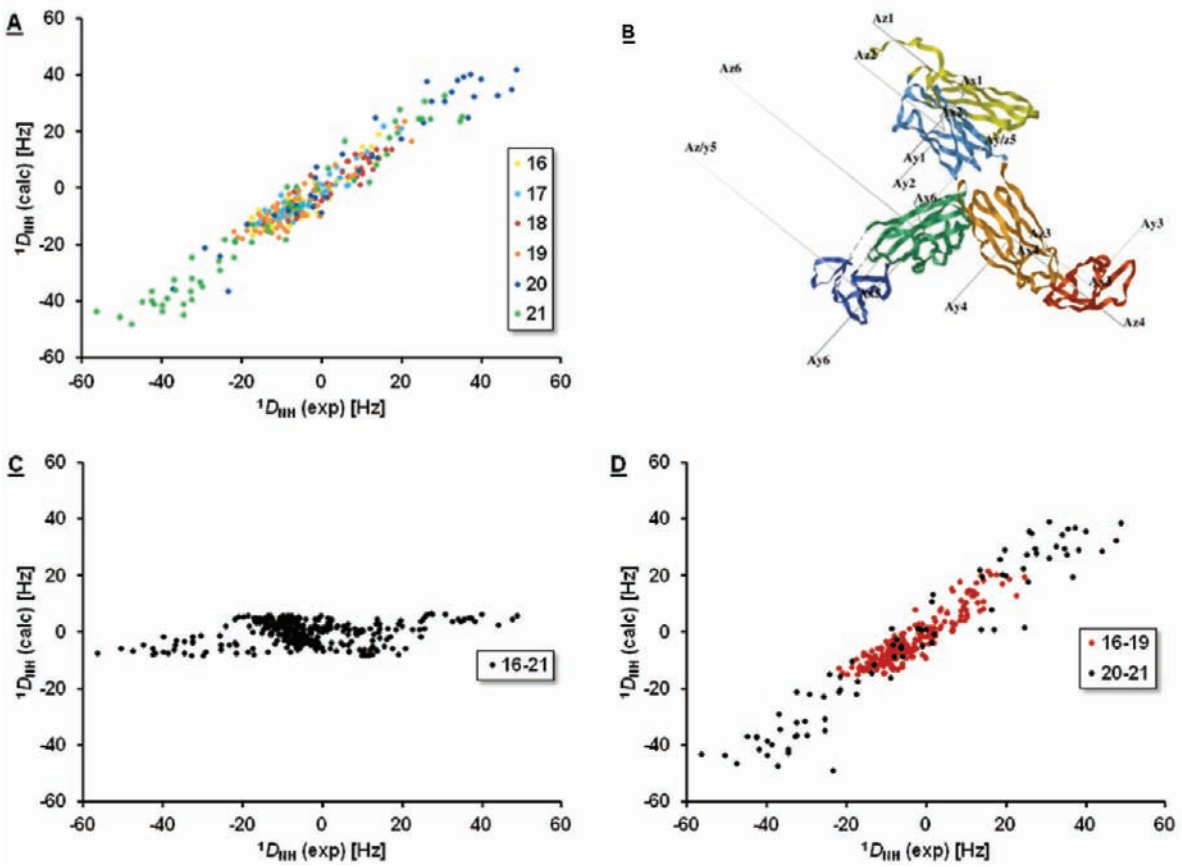

Figure 6. FLNa16−21 domain orientations using RDC restraints and rigid body modeling. (A) Linear correlations between experimental and back-calculated RDCs for the individual domains. (B) Resulting structure after colinearization of the alignment tensors of the individual domains. (C) Back-calculated linear correlation from structure 6B. (D) Linear correlation for domains 16−19 (red circles) and 20−21 separately. The figure in panel B was created with the MODULE program.[34]

interdomain interaction was also manifested as a wealth of 16−17 interdomain NOEs[19] in the structure.

The alignment tensors of domains 18 and 19 are mutually different. The extent of alignment of FLNa18 is weaker by a factor of ∼2, and the rhombicity (A_r/A_a) of its alignment tensor is at the maximum value. The Q factors obtained for the individual modules and the domain pair (Q = 0.45) suggest a domain orientation different from that observed in the NOE-based NMR structure.[19] The ensemble of FLNa18−19 structures indicates some flexibility between the domains, although relaxation data indicated tumbling as a single unit.[19] Reorientation of FLNa18 yields a pairwise Q of 0.40.

Experimental RDCs agree very well with individual domains 20 and 21. However, the Q factor is significantly higher for the domain pair (Q = 0.43), indicating that the RDC data also conflict with the domain orientation of the X-ray structure of FLNa19−21.[18] Reorientation of domain 20 yields a pairwise Q of 0.26.

The eigenvalues of the alignment tensor of domains 20 and 21 are considerably larger than those for domains 16−19, as evidenced by larger measured RDCs (Figure 5). In principle, distinct domain surface charge distributions and/or domain pair shapes could lead to distinct phage-protein interactions for the domain pairs. The program PALES[44,45] predicts, however, similar values for the magnitude of alignment: A_a for the domain pair 18−19 is 2.14×10^{-3} and for the domain pair 20−21 2.13×10^{-3} (at 25 °C, 15 mg/mL Pf1, 150 mM NaCl, pH 6.8).

We transferred the subunits into a common alignment frame. The 4-fold degeneracy in the possible combinations of domain orientations was eliminated by taking into account, in addition to the restrictions imposed by the covalent structure, the noncovalent restraints available from the existing structures of domain pairs and the chemical shift perturbation data. These data result in a model of FLNa16−21 in which the domain pairs have a propeller-shaped arrangement. Domains 17, 19, and 21 reside in the core whereas domains 16, 18, and 20 lie at the tips of the blades (Figure 6B).

In practice, only one plausible combination of degenerate orientations was found for the mutual orientation of FLNa16−17 and 18−19; all other combinations would have violated the covalent linkage between the domains or brought part of the structures into overlapping positions. The orientation possibilities of domain pairs 18−19 and 20−21 were more numerous but the orientation presented in Figure 6B supports the observed pattern of chemical shift differences. In the model presented the linkers between the domains 20 and 21 (residues A2150-P2151 and G2231-P2232) were allowed to distort in order to generate a structure in which an interdomain interface is created. As the domains tumble as a unit (see relaxation analysis below), a detectable interface is likely to exist. Evidence for the flexibility of these and surrounding residues comes from the high R_1 values and/or low NOEs and/or low R_2 values of S2152, V2153, and L2233, which are all in the connecting loops between domain pairs (see relaxation section below).

dx.doi.org/10.1021/ja2114882 | J. Am. Chem. Soc. 2012, 134, 6660−6672

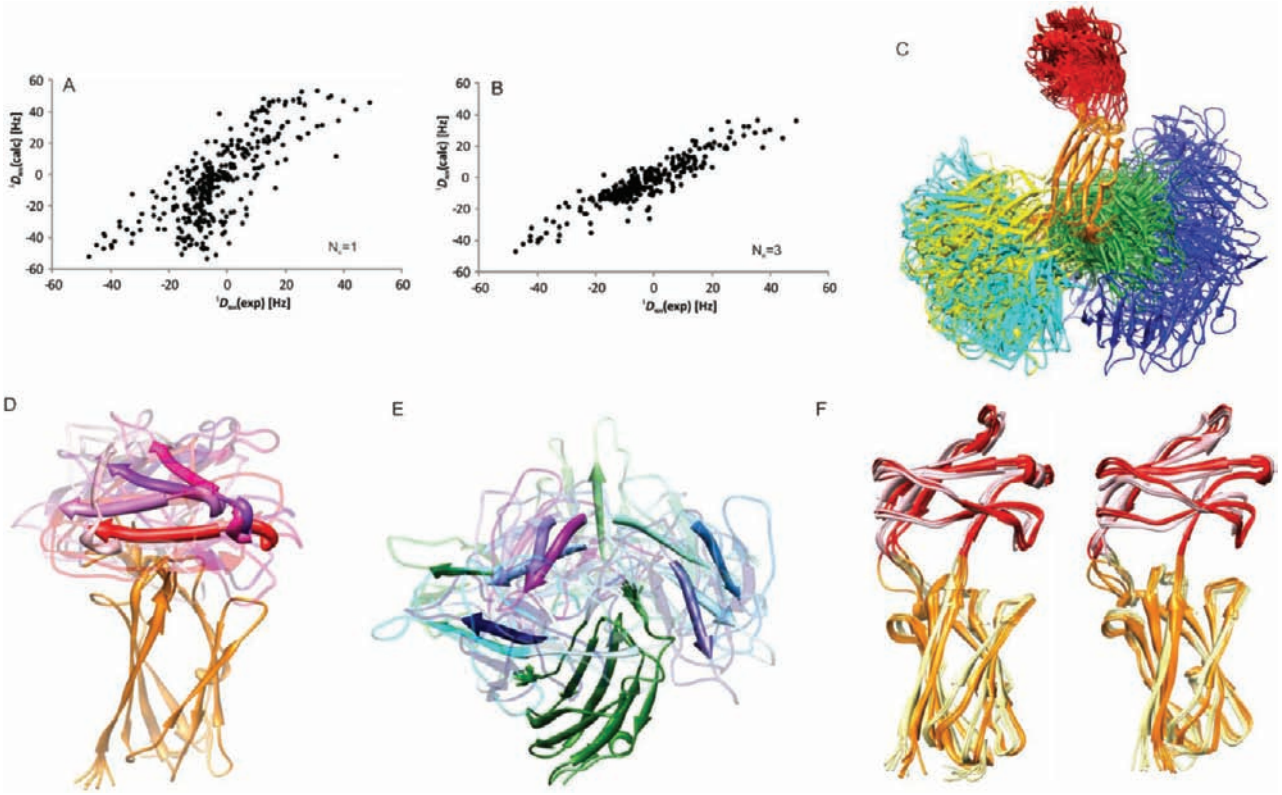

Figure 7. Ensemble simulation of FLNa16−21. Linear correlations for (A) ensemble size N_e = 1 and (B) N_e = 3. (C) Ten lowest-energy N_e = 3 ensembles with domains 19 superimposed. The domains are colored as in Fig. 6. In D) the relative orientations of domain 18 with respect to domain 19 are shown. To facilitate interpretation the region spanning residues 1980−1988 is highlighted and only one representative per orientation is shown. In (E) the relative orientations of domain 20 with respect to domain 21 are shown. The -strand spanning residues 2210−2214 is highlighted. The differences of structures within an ensemble can be appreciated from (F) where two main sets for domain pair 18−19, N_e = 2 are shown. One ensemble member is shown in dark colors and the other in light colors with domain 18 in shades of red. The five lowest-energy members of each set are shown. The structure figures were created with UCSF Chimera.[57]

After colinearization of the alignment tensor for individual domains, the *Q* factor (0.97) indicates a fit for the mutual orientation of domains 16−21 (Figure 6C) that gives no improvement over the initial FLNa16−21 model. However, if we assume that large interdomain motion occurs between the subunit composed of domains 16−19 and FLNa20−21 we obtain reasonably good fits: 16−19 *Q* = 0.38 and 20−21 *Q* = 0.26 (Figure 6D).

The generalized degree of order (ϑ, GDO) is a measure of the degree of alignment of individual domains.[46,47] For domains with collective motions equal values of ϑ are expected. Within the accuracy of the experiment, this is observed for FLNa16−17 (Table 1). The two other domain pairs have significantly different ϑs. The ratio of domain ϑs (ϑ_{int}, GDO_{int}) reports on the amplitude of interdomain motion.[46] Using the simplest motional model, motion in a cone,[48] ϑ_{int}(18−19) = 0.60 translates into an amplitude of interdomain motion Ψ_{cone} of 45°. Based on the ϑ_{int} values, interdomain motion is more pronounced between FLNa20−21 and the domain 19 than between FLNa16−17 and FLNa19: ϑ_{int}(19−20/21) are 0.62 and 0.55 (Ψ_{cone} = 44−49°) as compared to ϑ_{int}(19−16/17): 0.83−0.80 (Ψ_{cone} = 28−31°). The amplitude of motion is the smallest between FLNa20 and 21, Ψ_{cone} is 22°. These derived amplitudes of motion should be treated as lower limits of the actual motion.

This imposes an additional problem of nonuniform alignment; that is, rather than tumbling as a single rigid structural entity, described by a single molecular alignment tensor with all six domains in FLNa16−21 exhibiting identical or very similar values, the RDC data unambiguously indicate that there is significant interdomain motion between the domains of FLNa16−21.[25,49] The orientation of FLNa16−21 thus cannot be described using a single alignment tensor and distinct alignment tensors are required,.

Interdomain motion was explored by ensemble averaged structure calculations which have been shown to produce better fits between experimental and predicted RDCs.[50−52] Ideally one would compute the alignment tensor for each member of the ensemble during the structure calculation.[53−55] As this is difficult to fulfill in the case of electrostatic alignment (Pf1 phages) we used restrained molecular dynamics with the alignment tensor fitted to the measured RDCs.

Small angle adjustments may artificially produce good correlations between experimental and calculated RDCs.[56] Having only a limited $^1D_{NH}$ data set available, we chose to treat the individual domains 18−21 and FLNa 16−17 as rigid bodies. The relative motion of the rigid bodies was restrained by RDCs and radii of gyration for the domain pairs[19] and the domain sextet (Ruskamo et al., unpublished data). Additionally, the chemical shift perturbation data resulted in highly ambiguous NOE restraints[36] between residues 2085 and 2117 in domain 19 and residues 2276−2277, 2304, and 2306 in domain 21. The chemical shift differences observed for domain pair 16−17 were deemed not significant as they were scattered and relatively small. The best fit between experimental and back-calculated

dx.doi.org/10.1021/ja2114882 | *J. Am. Chem. Soc.* 2012, 134, 6660−6672

RDCs was obtained by fixing the values of D_a and R to those obtained from the histogram of RDCs (−27.0, 0.66).

A remarkable improvement of the fit between observed and back-calculated RDCs takes place when the number of structures in the ensemble is increased from one to two (Figure 7A,B). R_{dip} drops from 0.42 to 0.15, or the Q factor from 1.07 to 0.39. Increasing the number of ensemble members to three brings a further minute enhancement to the rms($D_{obs} - D_{calc}$), but R_{dip} remains the same. Ensemble size of four does not improve the fit further. R_{dip}/Q values for the individual domains in the lowest-energy N_e = 3 ensemble are 0.11/0.44 (domains 16−17), 0.12/0.51 (18), 0.13/0.40 (19), 0.26/0.43 (20), and 0.21/0.31 (21).

The ensemble simulations result in a three-branched structure in which the plausible domain orientations encompass a wide space (Figure 7C). The NOEs restrict the rotational freedom of FLNa21 relative to FLNa19 but FLNa16−17 efficiently explores the allowed conformational space within the limits of the relatively short linker between domains 17 and 18. For domain 20, relative domain orientations covering a ∼80° rotation angle relative to the long axis of FLNa21 or a shift from an orthogonal to a parallel position are observed (Figure 7E). For FLNa18 the overall rotation around the long axis of FLNa19 is as large, but no bending type of relative domain movement is observed (Figure 7D).

To further explore the dynamics of the interdomain motion in FLNa16−21, detected by the RDC measurements, we conducted NMR relaxation studies.

Dynamics in FLNa16−21. The nuclear spin relaxation is sensitive to molecular motion in the picosecond-nanosecond (ps-ns) time scales.[30,58] The longitudinal ^{15}N relaxation rate (R_1) and heteronuclear {^{1}HN}-^{15}N steady-state NOE in particular are sensitive to internal dynamics that take place in the fast ps-ns time scale whereas the transverse relaxation rate (R_2) is a reporter of both fast ps-ns motions and slow μs-ms dynamics. To characterize the dynamics of FLNa16−21, we measured backbone amide ^{15}N R_1 and R_2 relaxation rates as well as {^{1}HN}-^{15}N NOEs at a field strength of 18.79 T (Figure 8 and Table 2, see also Table S3 for the numerical listing of the relaxation data).

In general, the experimental R_1, R_2, and NOE values echo the secondary structure. Termini, loops, and domain linkers exhibit higher than average R_1s together with lower than average R_2s and NOEs, indicative of enhanced motion as compared to the core structure. The average R_1, R_2, and NOE values for domains 16−17 (Table 2) are in agreement with previous observations indicating that this part is a structural unit. Within the accuracy of the experiments, the motional properties of domains 20 and 21 are similar, and the overall tumbling is equivalent to that of FLNa16−17. R_{2avg} for domain 19 is higher and R_{1avg} lower than for FLNa16−17 and 20−21. Comparison of R_2/R_1 and $R_1 \times R_2$ plots,[60] which can be used to dissect chemical exchange from diffusion anisotropy, implies that domain 19 diffuses anisotropically (see Figures S4 and S5 for the R_2/R_1 and $R_1 \times R_2$ plots).

The average R_2/R_1 ratios of ∼60 (Table 2) correspond neither to those of FLNa16−21 tumbling as a propeller-shaped rigid body nor as individual domain pairs. HYDRONMR[61] predicts R_2/R_1 ratios of ∼430 and ∼20 for these structures, respectively. A globular shape can also be excluded, as it would result in a R_2/R_1 ratio of ∼80. Relaxation data measured for FLNa16−17 and 18−19 is in agreement with HYDRONMR predictions (see Figure S4 for the R_2/R_1 ratios of the pairs). Interestingly the pronounced anisotropic behavior of domain

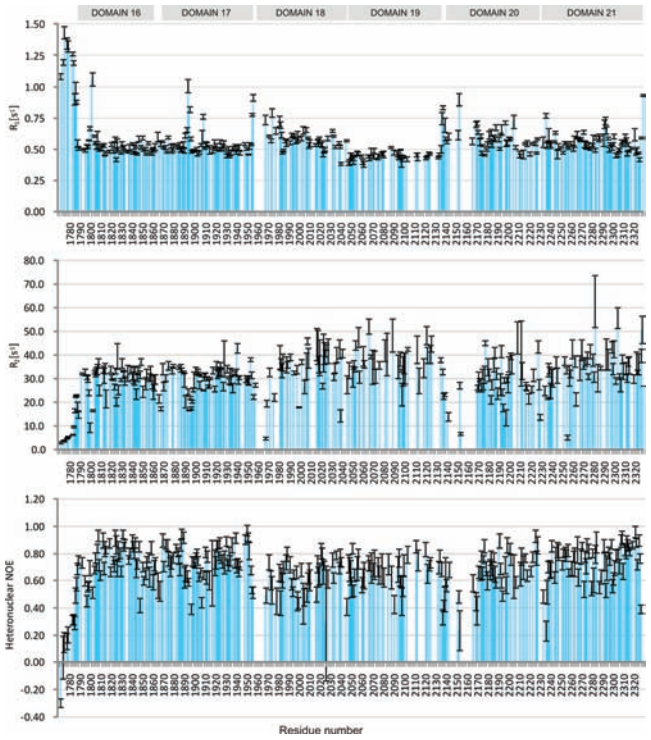

Figure 8. Backbone amide ^{15}N R_1 and R_2 relaxation rates and steady-state {^{1}HN}-^{15}N heteronuclear NOEs of FLNa16−21.

19 in FLNa16−21 is obscure in FLNa18−19. The increased anisotropy and the departure of the overall tumbling from either of the structures (pearls-on-a-string or rigid propeller) signify that domain pair motions are restricted by the interdomain interactions and/or the linkers and that interdomain motion is present. This result also confirms that sample perdeuteration and the use of TROSY were appropriate; it also excludes aggregation of FLNa16−21 as a contributor to the observed chemical shift perturbations between individual domain pairs and the six domain fragment.

Although the statistical uncertainty is large, it is intriguing to note that the rotational correlation times for domains 17, 19, and 21 (τ_c values ∼21.7, 25.3, and 21.4 ns, respectively) are, on average, larger than for domains 16, 18, and 20 (τ_cs ≈ 20.8, 22.4, and 20.5 ns, respectively), which is consistent with the structural model. The even-numbered domains at the tip of the blades have less restricted motional freedom compared to the inner, odd-numbered domains in the core of the propeller-like model. In general, the even-numbered domains also have somewhat lower heteronuclear NOEs than the odd-numbered domains. This is especially pronounced in the case of domain 18 and to some degree of domain 20; that is both have significant segments that display {^{1}HN}-^{15}N NOEs less than 0.65. Nevertheless, these data confirm the RDC data implying that FLNa16−21 does not tumble as a single rigid body; instead, there is significant independent tumbling of the domains. According to the relaxation and RDC data, FLNa16−17 form the most rigid domain pair, with more uniform dynamical features and mutual orientation between the domains as compared to those of FLNa18−19 and 20−21.

As noted previously, domain pair linker residues (1954−1957 and 2136−2139) have higher than average R_1s as well as lower than average R_2s and NOEs indicating mobility in the pico- to nanosecond time scale. However, residues 1958−1966

dx.doi.org/10.1021/ja2114882 | J. Am. Chem. Soc. 2012, 134, 6660−6672

Table 2. Average Values and Standard Deviations of FLNa16-21 Relaxation Parameters[a]

domain	R_1	R_2	NOE	R_2/R_1	τ_c
16	0.52 ± 0.05	29.6 ± 5.9	0.74 ± 0.18	57.1 ± 12.2	20.8 ± 2.5
17	0.52 ± 0.03	31.4 ± 3.5	0.75 ± 0.12	61.2 ± 8.0	21.7 ± 1.5
18	0.55 ± 0.07	36.5 ± 6.9	0.62 ± 0.13	67.1 ± 17.4	22.4 ± 3.2
19	0.45 ± 0.02	37.2 ± 4.3	0.68 ± 0.09	83.5 ± 9.7	25.3 ± 1.5
20	0.56 ± 0.06	30.7 ± 4.6	0.68 ± 0.14	56.2 ± 9.2	20.5 ± 1.9
21	0.55 ± 0.05	33.8 ± 4.8	0.73 ± 0.16	61.9 ± 10.8	21.4 ± 3.0

[a]Except for NOEs, residues with no significant contribution from internal motions have been taken into account when deriving the averages.[59]

and 2140−2149, corresponding to the A strands of domain 18 and 20, as well as residues from domain 19 facing the domain interface could not be assigned in FLNa16−21 (Figure 4). We suspect that line broadening due to micro- to millisecond chemical/conformational exchange causes the peaks to disappear. This is supported by the fact that all but one residue (for which data are available) in strands C, next to strands A, of domains 18 (2078−2086) and 20 (2269−2277), display larger than average R_2 values (with a mean of 39.9 ± 2.4 s^{-1}). For many residues in strand A of domain 18 the peaks were broad and the intensity too low to allow a reliable estimation of the relaxation rates.

A fit of the relaxation data to the model structure (Table 3) indicates that the domain pairs tumble anisotropically and that

Table 3. Domain Pair Diffusion Constants

	diffusion constant (ns)				
domain	$(6D_{xx})^{-1}$	$(6D_{yy})^{-1}$	$(6D_{zz})^{-1}$	Tr(D)	$\kappa_{\alpha\beta}$
FLNa16−17	21.1 ± 0.7	19.2 ± 0.7	16.3 ± 0.5	56.6	1.13
FLNa18−19	23.9 ± 1.3	21.4 ± 0.9	18.9 ± 0.9	64.2	
FLNa20−21	20.4 ± 1.1	17.4 ± 0.6	16.3 ± 0.7	54.1	1.19

FLNa 18−19 is the most restricted. As well as ϑ_{int}, the parameter $\kappa_{\alpha\beta}$ can be used as a measure of interdomain motion.[62] $\kappa_{\alpha\beta}$ is calculated as the ratio of diffusion matrix traces: $\kappa_{\alpha\beta}$ (18−19/16−17) is 1.13 and $\kappa_{\alpha\beta}$ (18−19/20−21) 1.19. Deviation from unity is a sign of interdomain motion on time scales similar to the overall rotational correlation time,[62] here ∼20 ns. The result is consistent with the RDC data in that thFLNa20−21 is the least restricted domain pair.

We employed reduced spectral density mapping (RSDM)[63,64] to analyze the relaxation data as this makes no assumptions about the molecular rotational diffusion. The results are shown in Figure 9, at three distinct frequencies, $0.87\omega_H$, ω_N, and 0 against the FLNa16−21 amino acid sequence. The high-frequency components $J(\omega_N)$, and especially $J(0.87\omega_H)$, are sensitive only to motions occurring on time scales faster than the overall tumbling, whereas $J(0)$ is sensitive to the overall rotational diffusion as well as chemical/conformational exchange on a slow μs-ms time scale. $J(0)$ values decrease as the nanosecond flexibility increases whereas $J(0.87\omega_H)$ values show the opposite behavior, that is an increase with increasing picosecond flexibility. For large proteins at high magnetic field $J(\omega_N)$ increases with increased flexibility. The N-terminus of FLNa16−21 is highly disordered as evidenced by high $J(\omega_N)$ and $J(0.87\omega_H)$ (up to 21.94 ± 0.67 ps/rad) and concomitant low $J(0)$ values for residues 1772−1787. Additional high-frequency motions albeit with a much smaller magnitude are observed for residues 1801, 1894−1898 and 1908 located in the BC loops of domains 16 and 17, and the CD loop of domain 17. Likewise, many of the loop residues

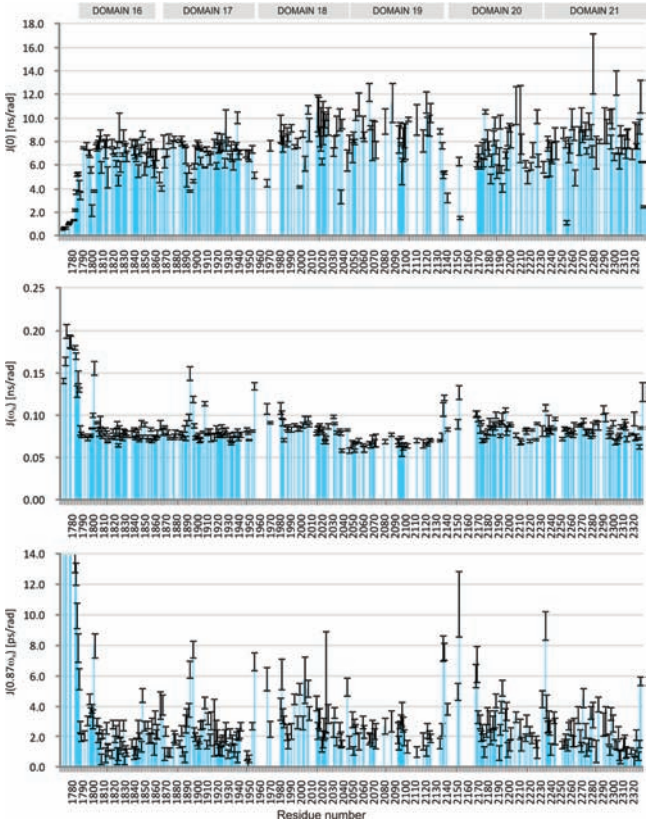

Figure 9. RSDM of FLNa16−21. The $J(0.87\omega_H)$ values of the flexible Nterminal tail (residues 1772−1783) are very large, up to 21.9 ps/rad, and were cut out for clarity.

in domains 18 and 20 display elevated picosecond dynamics, e.g., 1982, 2168−2169, and 2236 (up to 9.28 ± 0.93 ps/rad). A very large $J(0)$ value is an indication of slow exchange. Residues that have a $J(0)$ two standard deviations greater than the 10% trimmed mean value are 1826, 1928, 1940, 2066, 2088, 2121, 2177, 2207, 2281, 2303, and 2326. These are located in loops or at a position immediately succeeding the loop with the exception of 2177 located in the middle of strand C in domain 20. Domains 20 and 18 are the most dynamic, as indicated by the highest average $J(0.87\omega_H)$ and $J(\omega_N)$ values. The low $J(\omega_N)$ values observed for domain 19 reflect its restricted tumbling. FLNa18 is also mobile in the FLNa18−19 domain pair (see Figure S6 for domain pair 16−17 and 18−19 RSDM), its average $J(0.87\omega_H)$ value is 1.6 ps higher than those of domains 16 and 17 and 0.6 ps higher than that of domain 19. The average $J(\omega_N)$ value of domain 19 in the domain pair 18−19 is nearly equal to that of domain 18 (0.17 ns for domain 19 vs 0.16 ns for the three other domains).

dx.doi.org/10.1021/ja2114882 | J. Am. Chem. Soc. 2012, 134, 6660−6672

Interestingly, only slightly increased $J(0.87\omega_H)$ (4.08 ± 0.92 ps/rad) and significantly decreased $J(0)$ could be found for residues 1865−1867 located in the linker interconnecting domains 16 and 17. Low heteronuclear NOEs and R_2s were observed for linker residues prior to the A strand of domain 18 (residues 1954−1957). For residue 1956 this translates into elevated values of $J(0.87\omega_H)$ (6.94 ± 0.60 ps/rad) and $J(\omega_N)$ (0.13 ± 0.004 ns/rad) and a lowered value of $J(0)$ (5.19 ± 0.25 ns/rad). A similar behavior is observed for the linker residues between domains 19 and 20 (2136−2139) which exhibit increased mobility on ps time scale (up to 7.82 ± 0.83 ps/rad). Unfortunately it was not possible to obtain quantitative information on the dynamics of the A strands of domains 18 (residues 1958−1966) and 20 (residues 2140−2149) but they are likely to undergo slow conformational exchange on the micro- to millisecond time scales (see before).

DISCUSSION

In this study, we have used NMR spectroscopy to build a structural model of the domain arrangement in FLNa16−21. The model was constructed by combining NMR chemical shift perturbation maps, orientational restraints from RDC data and dynamical data from relaxation experiments with molecular architecture restraints and existing NMR and X-ray structures of domain pairs. The model consists of a propeller-like construction, where each domain-pair (16−17, 18−19, and 20−21) corresponds to one blade of the propeller. Motion between domains and domain pairs is substantial.

The interdomain dynamics is demonstrated by the scant chemical shift differences observed between FLNa16−21 and the domain pairs (Figures 3 and 4). Most of the differences are small, suggesting that no significant domain interactions stabilize the quaternary structure of FLNa16−21. Appreciable differences or peak disappearance are only observed for the domains 19 and 21, in the half of the protruding termini, indicating at least a transient interaction between these two domains.

Interdomain dynamics is also manifested in the RDC data. If FLNa16−21 tumbled as a single rigid body, with minimal interdomain movement, identical or very similar molecular alignment tensors would be obtained for each domain. On the contrary, the molecular alignment tensors determined for domains 20−21 differ significantly in terms of magnitude from those obtained for domains 16−19. Consequently, after parallelization of the individual alignment tensors, it was possible to obtain good fits for domain pairs 16−17, 18−19, and 20−21 as well as for the domain quartet 16−19 but not for the domain sextet 16−21 (Figure 6). The ϑ_{int} values indicate that the interdomain motion is more pronounced between the FLNa20−21 and FLNa19 than between the FLNa16−17 and FLNa19. As we do not observe significant chemical shift differences for FLNa16−17 this more limited motion must arise from restrictions in conformational space rather than from interdomain stabilizing interactions.

The ensemble simulation portrays a molecule with extensive interdomain motion but the three-branched propeller-shaped structure persists. Domains 18 and 20 show preferred orientations relative to domains 19 and 21. The number of unique orientations is nevertheless large, five (18−19) and more than ten (20−21) in the top ten N_e = 3 ensembles. This result is obtained with one type of RDC in one medium and reflects conformational sampling based on restrictions imposed by RDCs alone. It is conceivable that the number of orientations or the allowed conformational space reduces upon introduction of additional nonredundant RDC data or other structural restraints, e.g., NOE restraints between domains 18 and 19.[19]

Although we anticipate that the observed divergence in the molecular alignment of the fragments is due to the inherent dynamics of FLNa16−21, an explanation for the very different orientation strengths of FLNa16−19 and FLNa20−21 is unclear. All of the domains in FLNa16−21 are of similar size and amino acid composition, suggesting that the orientations of individual domains should be similar if the alignment arose purely from steric effects. Differences could arise from nonuniform electrostatic interactions with the filamentous phage in the RDC alignment medium. While this could in principle be assessed by measuring RDC in an alignment medium with significantly different alignment tensors to those obtained with filamentous phage, trials to measure RDCs in bicelles induced large chemical shift perturbations, severe line broadening and disappearance of several cross peaks, preventing analysis of RDCs in a bicelle medium.

Interdomain dynamics is also evident from the ^{15}N relaxation data. The overall rotational correlation times for different domains in FLNa16−21 deviate noticeably from those predicted for a rigid propeller-like construction with a molecular weight of 60 kDa. The motion is, however, restricted as the correlation times are considerably larger than those calculated for domains tumbling individually. We observed significantly higher R_2/R_1 values for the domain 19 and concomitant close-to-average $R_1 \times R_2$ values which indicates that this domain tumbles anisotropically. The diffusion constants suggest that the anisotropy originates from the restricted tumbling of FLNa19. Given that $J(\omega_N)$ values of the flanking domains are higher we reason that these domains undergo interdomain motion relative to domain 19 that is of the order of the overall tumbling rate.

The model assembled using NMR spectrosopy is in agreement with small-angle X-ray (SAXS) data acquired from the same fragment (Ruskamo et al., unpublished results). These SAXS data reveal a three-branched structure with a maximum linear dimension, D_{max}, of 12 nm. In our model, the maximum distance measured from the N-terminus to the tip of domain 18 is 11.7 nm. However, both the ^{15}N backbone relaxation data and the perception given by the RDC data clearly indicate that interdomain flexibility is an intrinsic property of the FLNa16−21 fragment. Although the linkers between the domains are relatively short, restricting the conformational sampling of the domains, they still leave room for interdomain flexibility.

The relaxation data also indicate that the A strands of domains 18 and 20 are mobile in the slow micro- to millisecond time scale. The mechanism of interaction between FLNa and integrin has been studied by steered molecular dynamics simulations.[65] It was proposed that mechanical force applied to filamin would lead to the exposure of the integrin binding site. The binding site resides on the CD-face which is masked by the A strand. The μs-ms mobility observed in strands A might loosen the strand so as to decrease the force needed to detach it from the domain.

Functional Implications. The short covalent linker sequences between domain pairs are expected to restrict the conformational freedom in the intact molecule. Transformation of the alignment tensors to a common alignment frame indicates that the domain pairs arrange into a clover-leaf-shaped structure. The RDC and relaxation data show that FLNa20−21

dx.doi.org/10.1021/ja2114882 | J. Am. Chem. Soc. 2012, 134, 6660−6672

exhibits large amplitude interdomain motion with respect to the domain quartet 16−19. In addition, flexibility is observed between domains 18 and 19 as well as 20 and 21. The faster transverse relaxation of domains 17, 19, and 21 implies that these domains form the core of the FLNa16−21 fragment. In this domain organization, the interaction sites at the CD faces of domains 17, 19, and 21 are exposed to solvent and available for interactions.[65]

CONCLUSIONS

We have structurally characterized FLNa16−21 a 60-kDa fragment of filamin A, using RDC restraints and the structures of FLNa domain pairs 16−17, 18−19, and 20−21. Extensive backbone sequential assignment of FLNa16−21 was achieved by comparing the spectra of FLNa16−21 to the spectra of the subcomponents. The structure model conforms to SAXS data acquired from the same FLNa construct. Our results imply that NMR spectroscopy, in terms of residual dipolar couplings, chemical shift perturbations and ^{15}N autorelaxation rates, provides a powerful way of studying relatively large and intrinsically dynamic multidomain proteins that are challenging to crystallize.

ASSOCIATED CONTENT

Supporting Information

Figures displaying ^{1}H, ^{15}N HSQC of FLNa20−21 with chemical shift assignment for NH resonances, experimental/structural model R_2/R_1 ratios as a function of the amino acid sequence, $R_1 \times R_2$ plot of FLNa16−21, and RSDM of FLNa16−17, 18−19. Tables of FLNa16−21 N−H chemical shift assignments, FLNa16−21 experimental RDCs as well as ^{15}N R_1, R_2, and NOE relaxation data. This material is available free of charge via the Internet at http://pubs.acs.org.

AUTHOR INFORMATION

Corresponding Author

Perttu.Permi@helsinki.fi

Author Contributions

[#]These authors contributed equally to this work.

Notes

The authors declare no competing financial interest.

ACKNOWLEDGMENTS

This work was supported by the Academy of Finland Grants 122170 and 131144 for P.P. and BBSRC for I.D.C. P.J. is partly supported by NSFC (No. 31100530). We acknowledge CSC−IT Center for Science Ltd. for the allocation of computational resources.

REFERENCES

(1) van der Flier, A.; Sonnenberg, A. *Biochim. Biophys. Acta* **2001**, *1538*, 99−117.
(2) Feng, Y.; Walsh, C. A. *Nat. Cell Biol.* **2004**, *6*, 1034−1038.
(3) Robertson, S. P. *Curr. Opin. Genet. Dev.* **2005**, *15*, 301−307.
(4) Zhou, X.; Tian, F.; Sandzén, J.; Cao, R.; Flaberg, E.; Szekely, L.; Cao, Y.; Ohlsson, C.; Bergo, M. O.; Borén, J.; Akyürek, L. M. *Proc. Natl. Acad. Sci. U.S.A.* **2007**, *104*, 3919−3924.
(5) Popowicz, G. M.; Schleicher, M.; Noegel, A. A.; Holak, T. A. *Trends Biochem. Sci.* **2006**, *31*, 411−419.
(6) Gorlin, J. B.; Yamin, R.; Egan, S.; Stewart, M.; Stossel, T. P.; Kwiatkowski, D. J.; Hartwig, J. H. *J. Cell. Biol.* **1990**, *111*, 1089−1105.
(7) Pudas, R.; Kiema, T.; Butler, P. J. G.; Stewart, M.; Ylänne, J. *Structure* **2005**, *13*, 111−119.
(8) Clark, A. R.; Sawyer, G. M.; Robertson, S. P.; Sutherland-Smith, A. J. *Hum. Mol. Genet.* **2009**, *18*, 4791−4800.
(9) Sawyer, G. M.; Clark, A. R.; Robertson, S. P.; Sutherland-Smith, A. J. *J. Mol. Biol.* **2009**, *390*, 1030−1047.
(10) Hartwig, J. H.; Tyler, J.; Stossel, T. P. *J. Cell. Biol.* **1980**, *87*, 841−848.
(11) Kiema, T.; Lad, Y.; Jiang, P.; Oxley, C. L.; Baldassarre, M.; Wegener, K. L.; Campbell, I. D.; Ylänne, J.; Calderwood, D. A. *Mol. Cell* **2006**, *21*, 337−347.
(12) Nakamura, F.; Pudas, R.; Heikkinen, O.; Permi, P.; Kilpeläinen, I.; Munday, A. D.; Hartwig, J. H.; Stossel, T. P.; Ylänne, J. *Blood* **2006**, *107*, 1925−1932.
(13) Lad, Y.; Jiang, P.; Ruskamo, S.; Harburger, D. S.; Ylänne, J.; Campbell, I. D.; Calderwood, D. A. *J. Biol. Chem.* **2008**, *283*, 35154−35163.
(14) Takala, H.; Nurminen, E.; Nurmi, S. M.; Aatonen, M.; Strandin, T.; Takatalo, M.; Kiema, T.; Gahmberg, C. G.; Ylänne, J.; Fagerholm, S. C. *Blood* **2008**, *112*, 1853−1862.
(15) Ithychanda, S. S.; Das, M.; Ma, Y.; Ding, K.; Wang, X.; Gupta, S.; Wu, C.; Plow, E. F.; Qin, J. *J. Biol. Chem.* **2009**, *284*, 4713−4722.
(16) Popowicz, G. M.; Müller, R.; Noegel, A. A.; Schleicher, M.; Huber, R.; Holak, T. A. *J. Mol. Biol.* **2004**, *342*, 1637−1646.
(17) Nakamura, F.; Osborn, T. M.; Hartemink, C. A.; Hartwig, J. H.; Stossel, T. P. *J. Cell. Biol.* **2007**, *179*, 1011−1025.
(18) Lad, Y.; Kiema, T.; Jiang, P.; Pentikäinen, O. T.; Coles, C. H.; Campbell, I. D.; Calderwood, D. A.; Ylänne, J. *EMBO J.* **2007**, *26*, 3993−4004.
(19) Heikkinen, O.; Ruskamo, S.; Konarev, P. V.; Svergun, D. I.; Iivanainen, T.; Heikkinen, S. M.; Permi, P.; Koskela, H.; Kilpeläinen, I.; Ylänne, J. *J. Biol. Chem.* **2009**, *284*, 25450−25458.
(20) Nakamura, F; Stossel, T. P.; Hartwig, J. H. *Cell Adh. Migr.* **2011**, *5*, 160−9.
(21) Pickford, A. R.; Campbell, I. D. *Chem. Rev.* **2004**, *104*, 3557−3566.
(22) Pervushin, K.; Riek, R.; Wider, G.; Wüthrich, K. *Proc. Natl. Acad. Sci. U.S.A.* **1997**, *94*, 12366−71.
(23) Bertini, I.; Del Bianco, C.; Gelis, I.; Katsaros, N.; Luchinat, C.; Parigi, G.; Peana, M.; Provenzani, A.; Zoroddu, M. A. *Proc. Natl. Acad. Sci. U. S. A.* **2004**, *101*, 6841−6846.
(24) Volkov, A. N.; Worrall, J. A.; Holtzmann, E.; Ubbink, M. *Proc. Natl. Acad. Sci. U.S.A.* **2006**, *103*, 18945−18950.
(25) Fischer, M. W.; Losonczi, J. A.; Weaver, J. L.; Prestegard, J. H. *Biochemistry* **1999**, *38*, 9013−9022.
(26) Skrynnikov, N. R. *C. R. Physique* **2004**, *5*, 359−375.
(27) Blackledge, M. *Prog. Nucl. Magn. Reson. Spectrosc.* **2005**, *46*, 23−61.
(28) Mäntylahti, S.; Koskela, O.; Jiang, P.; Permi, P. *J. Biomol. NMR* **2010**, *47*, 183−194.
(29) Goddard, T. D.; Kneller, D. G. *Sparky 3*; University of California: San Francisco, CA, 2004.
(30) Farrow, N. A.; Muhandiram, R.; Singer, A. U.; Pascal, S. M.; Kay, C. M.; Gish, G.; Shoelson, S. E.; Pawson, T.; Forman-Kay, J. D.; Kay, L. E. *Biochemistry* **1994**, *33*, 5984−6003.
(31) Zhu, G.; Xia, Y.; Nicholson, L. K.; Sze, K. H. *J. Magn. Reson.* **2000**, *143*, 423−426.
(32) Dosset, P.; Hus, J-C; Blackledge, M.; Marion, D. *J. Biomol. NMR* **2000**, *16*, 23−28.
(33) Hansen, M. R.; Mueller, L.; Pardi, A. *Nat. Struct. Biol.* **1998**, *5*, 1065−1074.
(34) Dosset, P.; Hus, J.-P.; Marion, D.; Blackledge, M. *J. Biomol. NMR* **2001**, *20*, 223−231.
(35) Schwieters, C. D.; Kuszewski, J. J.; Clore, G. M. *Prog. Nucl. Mag. Res. Sp.* **2006**, *48*, 47−62.
(36) Clore, G. M.; Schwieters, C. D. *J. Am. Chem. Soc.* **2003**, *125*, 2902−2912.
(37) Heikkinen, O.; Permi, P.; Koskela, H.; Ylänne, J.; Kilpeläinen, I. *Biomol. NMR Assign.* **2009**, *3*, 53−56.
(38) Tjandra, N.; Bax, A. *Science* **1997**, *278*, 1111−1114.

(39) Tugarinov, V.; Choy, W. Y.; Orekhov, V. Y.; Kay, L. E. *Proc. Natl. Acad. Sci. U.S.A.* **2005**, *102*, 622−627.
(40) Tolman, J. R.; Flanagan, J. M.; Kennedy, M. A.; Prestegard, J. H. *Proc. Natl. Acad. Sci. U.S.A.* **1995**, *92*, 9279−9283.
(41) Annila, A.; Permi, P. *Concepts Magn. Reson. Spectr.* **2004**, *23A*, 22−37.
(42) Cornilescu, G.; Marquardt, J. L.; Ottiger, M.; Bax, A. *J. Am. Chem. Soc.* **1998**, *120*, 6836−6837.
(43) Clore, G. M.; Garrett, D. S. *J. Am. Chem. Soc.* **1999**, *121*, 9008−9012.
(44) Zweckstetter, M.; Bax, A. *J. Am. Chem. Soc.* **2000**, *122*, 3791−3792.
(45) Zweckstetter, M.; Hummer, G.; Bax, A. *Biophys. J.* **2004**, *86*, 3444−3460.
(46) Tolman, J. R.; Al-Hashimi, H. M.; Kay, L. E.; Prestegard, J. H. *J. Am. Chem. Soc.* **2001**, *123*, 1416−1424.
(47) Yuwen, T.; Post, C. B.; Skrynnikov, N. R. *J Biomol. NMR* **2011**, *51*, 131−150.
(48) Tolman, J. R.; Flanagan, J. M.; Kennedy, M. A.; Prestegard, J. H. *Nat. Struct. Biol.* **1997**, *4*, 292−297.
(49) Braddock, D. T.; Cai, M.; Baber, J. L.; Huang, Y.; Clore, G. M. *J. Am. Chem. Soc.* **2001**, *123*, 8634−8635.
(50) Clore, G. M.; Schwieters, C. D. *J. Am. Chem. Soc.* **2004**, *126*, 2923−2938.
(51) Clore, G. M.; Schwieters, C. D. *Biochemistry* **2004**, *43*, 10678−10691.
(52) Clore, G. M.; Schwieters, C. D. *J. Mol. Biol.* **2006**, *355*, 879−886.
(53) Esteban-Martín, S.; Fenwick, R. B.; Salvatella, X. *J. Am. Chem. Soc.* **2010**, *132*, 4626−4632.
(54) Huang, J.; Grzesiek, S. *J. Am. Chem. Soc.* **2010**, *132*, 694−705.
(55) De Simone, A.; Montalvao, R. W.; Vendruscolo, M. *J. Chem. Theory Comput.* **2011**, *7*, 4189−4195.
(56) Bax, A.; Grishaev, A. *Curr. Opin. Struct. Biol.* **2005**, *15*, 563−570.
(57) Pettersen, E. F.; Goddard, T. D.; Huang, C. C.; Couch, G. S.; Greenblatt, D. M.; Meng, E. C.; Ferrin, T. E. *J. Comput. Chem.* **2004**, *25*, 1605−12.
(58) Kay, L. E. *Nat. Struct. Biol.* **1998**, *5*, 513−517.
(59) Tjandra, N.; Feller, S. E.; Pastor, R. W.; Bax, A. *J. Am. Chem. Soc.* **1995**, *117*, 12562−12566.
(60) Kneller, J. M.; Lu, M.; Bracken, C. *J. Am. Chem. Soc.* **2002**, *124*, 1852−1853.
(61) García de la Torre, J.; Huertas, M. L.; Carrasco, B. *J. Magn. Reson.* **2000**, *147*, 138−146.
(62) Brüschweiler, R.; Liao, X.; Wright, P. E. *Science* **1995**, *268*, 886−889.
(63) Peng, J. W.; Wagner, G. *Biochemistry* **1992**, *31*, 8571−86.
(64) Farrow, N. A; Zhang, O.; Szabo, A.; Torchia, D. A.; Kay, L. E. *J. Biomol. NMR* **1995**, *6*, 153−62.
(65) Pentikäinen, U.; Ylänne, J. *J. Mol. Biol.* **2009**, *393*, 644−657.